*buildings*

MDPI

*Article*

# Autogenous and Chemical Shrinkage of Limestone Calcined Clay Cement ($LC^3$) Pastes

**Emily Canda [1,*], Rackel San Nicolas [2], Haleh Rasekh [1] and Arnaud Castel [1]**

[1] School of Civil and Environmental Engineering, University of Technology Sydney (UTS), Sydney, NSW 2007, Australia; haleh.rasekh@uts.edu.au (H.R.)
[2] Department of Infrastructure Engineering, University of Melbourne (UoM), Melbourne, VIC 3010, Australia
* Correspondence: emily.canda@uts.edu.au

**Abstract**

This study investigated the chemical and autogenous shrinkage behaviour of limestone calcined clay cement ($LC^3$) pastes incorporating calcined clays sourced from Australia, France, and India. Hydration development and microstructural evolution were examined using X-ray diffraction (XRD), Fourier-transform infrared spectroscopy (FTIR), thermogravimetric analysis (TGA), and pore-size distribution analysis. Results showed that $LC^3$ mixes hydration accelerates during early phases, with the main silicate hydration peak appearing more prominently than that in the GP and FA reference pastes, indicating increased nucleation and growth of hydration products due to the limestone filler effect. $LC^3$ pastes exhibited higher autogenous shrinkage overtime, strongly influenced by calcined clay reactivity and particle fineness. A clear correlation was observed between pore refinement and autogenous deformation during the early phases (7 days): pastes with a greater volume of fine pores showed higher early-age autogenous shrinkage during the first 7 days of hydration. In contrast, the chemical shrinkage of $LC^3$ mixes was comparable to that of the GP and FA systems at early ages ($\leq$7 days) but became lower after 28 days, attributed to both the matrix densification and additional nucleation sites provided by the limestone. Overall, $LC^3$ reduces long-term chemical shrinkage and densifies the microstructure; however, the refined pore structure and increased internal water demand lead to higher autogenous shrinkage. These findings demonstrate a direct link between hydration-driven microstructural evolution (phase formation and pore refinement) and the resulting shrinkage behaviour.

**Keywords:** limestone calcined clay cement; chemical shrinkage of cement; autogenous shrinkage of cement; structural performances of cement pastes



Academic Editor: Geo Paul

Received: 13 October 2025
Revised: 7 November 2025
Accepted: 10 November 2025
Published: 13 November 2025

**Citation:** Canda, E.; San Nicolas, R.; Rasekh, H.; Castel, A. Autogenous and Chemical Shrinkage of Limestone Calcined Clay Cement ($LC^3$) Pastes. *Buildings* **2025**, *15*, 4089. https://doi.org/10.3390/buildings15224089



## 1. Introduction

Concrete is widely used in the construction industry due to its affordability and ease of use on-site [1]. However, the production of concrete contributes significantly to $CO_2$ global emissions. The majority of these emissions are generated during the manufacturing process of cement through the calcination of the raw materials [2].

Numerous researchers have conducted investigations on a wide range of supplementary cementitious materials (SCMs) to reduce $CO_2$ emissions [3–6]. In the construction materials market, several SCMs have been extensively studied and are currently being consistently utilised. Among these materials are fly ash (FA) (which is derived from coal-fired power plants) and ground granulated blast-furnace slag (a by-product of the blast

furnace process) [6]. These two materials replace calculated portions of traditional cement, thereby decreasing the reliance and percentage of ordinary Portland cement (OPC). FA and slag are widely used in the construction industry and have been relied on as a sustainable alternative to cement for decades; however, it is projected that there will be a decrease in the availability of FA in the future due to a shift from coal-based manufacturing processes towards alternative fuels due to industries adopting more sustainable methods [7]. As industries increasingly adopt and convert to more sustainable processes, there will likely be a decline in the supply of both FA and slag as SCMs. The reduction in the availability of slag can mainly be attributed to the transition from blast furnaces to arc furnaces that utilise scrap steel instead of iron [8].

To address the upcoming shortages, researchers have explored alternative materials to meet the demand for more accessible SCMs. One such material is clay, which makes up a considerable portion of the earth's crust. When clays are calcinated, they become pozzolanic and undergo reactions between $AS_2$ ($Al_2O_3 \cdot 2SiO_2$) and $Ca(OH)_2$ compounds as seen in Equation (1) [9].

$$Al_2Si_2O_7 + 3Ca(OH)_2 + 5H_2O \rightarrow CaSiO_3 \cdot H_2O + 2Al(OH)_3 \quad (1)$$

Once calcined, it is then referred to as calcined clay, as there may not be enough kaolinite/meta-kaolin content to refer to the material as "meta-kaolin". Instead, calcined clay is a material with various minerals that has been calcined and transformed.

In previous studies, it was demonstrated that both calcined clay and limestone have the potential to replace OPC [3,4]. Similar to pozzolans, when exposed to calcium hydroxide, reactive calcined kaolinite in calcined clay reacts by producing C-A-S-H (calcium alumino-silicate hydrate), aluminate hydrates, ettringite, and occasionally stratlingite. The incorporation of aluminium into C-A-S-H increases as the amount of available calcined kaolinite content increases. The addition of limestone adds an extra filler material and also reacts with aluminate from calcined clay to form pore-filling carboaluminates (Equation (2)) [9].

The equation for limestone and aluminates forming monocarboaluminate is as follows:

$$4C_aO \cdot Al_2O_3 \cdot SO_3 \cdot 12H_2O + CaCO_3 + 2H_2O \rightarrow 4CaO \cdot Al_2O_3 \cdot CaCO_3 \cdot 11H_2O + CaSO_4 \cdot 2H_2O \quad (2)$$

According to research, it has been found that a kaolinite content of 40% in the clay before being calcined is sufficient to produce concrete with a mechanical strength comparable to that of OPC-based concrete [10]. There have been numerous studies conducted using different types of calcined clays, although limited attention has been given to the issue of shrinkage in limestone calcined clay cement ($LC^3$). It is crucial to examine the chemical and autogenous shrinkage of $LC^3$ pastes when compared with conventional OPC and blended pastes. High early-age shrinkage has the potential to cause cracks in cement paste and concrete, leading to mechanical and durability issues. Several factors can influence shrinkage behaviour, including changes in binder types, replacement of cement with additives, fineness of binders, and curing conditions [11–14]. Shrinkage is typically categorised into several types: drying shrinkage, plastic shrinkage, autogenous shrinkage, thermal shrinkage, and carbonation shrinkage. Drying shrinkage occurs due to water loss to the environment, while autogenous shrinkage is driven by self-desiccation resulting from hydration. Under sealed conditions, self-desiccation generates stress on pore walls that lead to autogenous shrinkage. Self-desiccation and autogenous shrinkage also occur in unsealed conditions, although there will also be drying shrinkage due to exposure to the elements [15].

An investigation on the autogenous shrinkage of $LC^3$ mixes that compared them to conventional OPC-based concretes showed that $LC^3$ concretes demonstrate increased autogenous shrinkage at later stages, which can be attributed to the refinement of pore structure within these materials [11]. Additionally, Afroz (2022) conducted research specifically on aluminosilicate blends by comparing FA with $LC^3$ mixtures, and both findings from the studies indicated that $LC^3$ blends exhibit significantly higher levels of autogenous shrinkage due to their faster hydration kinetics and greater pozzolanic reactivity [16].

Understanding the relationship between pore structure characteristics and material reactivity is crucial when autogenous shrinkage in concrete is being considered. Numerous studies have consistently shown that these factors play a significant role in determining the magnitude of autogenous shrinkage [13,17–19]. The porosity and connectivity of capillary pores greatly influence how water diffuses through the concrete matrix, impacting both drying shrinkage and self-induced (autogenous) shrinkage. A previous study conducted by Ston (2019) indicated that calcined clays can modify pore structures and mitigate autogenous shrinkage to some extent [13]. Calcined clay has been found to be effective in reducing early-stage autogenous shrinkage but may contribute to higher long-term autogenous shrinkage as investigated by various researchers [11,12,16,20]. Additionally, fillers are generally known for decreasing overall shrinkage by acting as small aggregates within the cement paste, which limits the number of voids susceptible to shrinking [21]. However, there is limited research exploring the role of calcined clay as a filler, particularly in the context of autogenous shrinkage. Most studies have focused on it pozzolanic reactivity rather than its physical role in shrinkage mitigation. This represents a key gap in the literature. This research addresses this gap by investigating whether modifying the particle size of calcined clay acts as both a filler and a SCM leading to a reduction of shrinkage.

In this study, the investigation focused on different types of calcined clay, each with distinct reactivity and physical characteristics related to shrinkage. By analysing parameters such as kaolinite content, amorphous phase content, and pore size distribution, this research aimed to understand the relationship between the material properties and shrinkage behaviour. By clarifying how specific calcined clay properties influence shrinkage behaviour, this study explored the potential to manipulate these characteristics to optimise the material's physical performance in sustainable concrete.

## 2. Materials and Methods

To conduct a comprehensive analysis of paste samples, several materials were employed. A total of nine different materials were utilised for various analyses including X-ray diffraction (XRD), isothermal calorimetry, thermogravimetric analysis (TGA), X-ray fluorescence (XRF), pore-size analysis, and autogenous shrinkage measurements.

The selected materials include General Purpose (GP) cement, which complied with AS 3972 standards [22]. Additionally, commercial class F FA was used. Fine limestone Omyacarb© (Omya, Oftringen, Switzerland) was also used in the paste mix along with six calcined clays: ICC from India; FCC from France; and ACC, BCC, CCC, and DCC from Australia.

The characteristics of the selected calcined clays for this study are outlined in Table 1. Two of these calcined clays, namely ICC and FCC, were utilised in previous studies [23].

Particle-size distribution measurements were conducted by laser diffraction utilising the wet method at the University of Technology Sydney (UTS) Tech Lab. Additionally, nitrogen absorption with the Blaine method and Brunauer–Emmett–Teller (BET) technique was used to measure the surface area of the different calcined clays (Table 1).

Before experiments were conducted, all Australian clays were characterised before and after calcination [24].

**Table 1.** The properties of various calcined clays.

| Clay Name | Calcined Clay Name | Kaolinite Content (%) | Amorphous Quantification (%) | PSD (%) | | | BET Surface Area ($m^2/g$) |
|---|---|---|---|---|---|---|---|
| | | | | 10v (10% Passing the Below Micron (μm)) | 50v (50% Passing the Below Micron (μm)) | 90v (90% Passing the Below Micron (μm)) | |
| - | ICC | - | 73.4 | 3.8 | 14.4 | 43.3 | 8.8 |
| - | FCC | - | 56.2 | 2.5 | 21.1 | 64.7 | 12.5 |
| ARC | ACC | 44.7 | 46.1 | 2.7 | 14.5 | 86.4 | 11.4 |
| BRC | BCC | 44.3 | 66.5 | 3.5 | 31.1 | 111.0 | 31.8 |
| CRC | CCC | 35.7 | 65.3 | 2.6 | 12.7 | 51.8 | 15.8 |
| DRC | DCC | 35.0 | 53.5 | 3.3 | 28.3 | 112.0 | 33.7 |
| Limestone | - | - | - | 7.7 | 43.3 | 130.5 | - |

The quantification of the amorphous phase in all calcined clays was determined by XRD using the external Rietveld analysis method and anatase as the reference sample. This analysis was performed using the Bruker D8 Discover X-ray diffractometer with copper (Cu) as the source material and a fixed slit size of 0.5°, sourced from Bruker AXS GmbH, Karlsruhe, Germany. The rotation range of the analysis was investigated from 5 to 70° 2θ, with a step size of 0.026° 2θ. The characterisation and analysis of each selected clay's mineralogy was performed utilising Highscore Plus (v5.2) (Table 2). Due to proprietary reasons, the chemical compositions of the Portland cement and FA are not included. These materials comply with the relevant Australian Standards AS 3972 for cement and AS 3582.1 for fly ash) [22,25].

**Table 2.** Simplified phases present in the calcined clays analysed via XRD.

| Sample | CaO | $SiO_2$ | $Al_2O_3$ | $Fe_2O_3$ | $SO_3$ | MgO | $K_2O$ | $TiO_2$ | $Na_2O$ | $P_2O_5$ | $Mn_2O_3$ | LOI | Total + LOI | Moisture |
|---|---|---|---|---|---|---|---|---|---|---|---|---|---|---|
| ICC | 0.14 | 48.4 | 41.75 | 2.25 | 0.11 | 0.05 | 0.05 | 3.38 | 0.23 | 0.08 | 0.01 | 3.33 | 99.78 | 0.35 |
| FCC | 0.49 | 74.5 | 19.28 | 2.04 | 0.03 | 0.11 | 0.17 | 0.95 | 0.03 | 0.04 | 0.01 | 2.17 | 99.82 | 0.54 |
| ACC | 1.08 | 58.08 | 23.01 | 9.27 | 0.17 | 1.4 | 2.59 | 0.89 | 0.07 | 0.48 | 0.18 | 2.58 | 99.8 | 0.64 |
| BCC | 2.4 | 42.22 | 23.88 | 18.73 | 0.04 | 3.43 | 0.52 | 2.71 | 0.76 | 0.28 | 0.2 | 4.94 | 100.11 | 1.45 |
| CCC | 0.1 | 65.92 | 19.64 | 5.59 | 0.08 | 0.7 | 2.27 | 0.75 | 0.37 | 0.03 | 0.12 | 4.12 | 99.69 | 1.36 |
| DCC | 4.94 | 56.46 | 14.23 | 9.69 | 0.07 | 3.4 | 1.19 | 1.44 | 1.16 | 0.12 | 0.11 | 6.99 | 99.8 | 1.79 |
| Limestone | 57.51 | 0.36 | 0.11 | 0.1 | - | 0.29 | - | - | - | - | - | - | - | - |

The TGA Mettler Toledo TGA/DSC 2 at UTS Tech Lab, with a high-temperature range of 50–1150 °C, a heating rate of 10 °C per minute, and a gas flow rate of 50 mL/min, was used to confirm the kaolinite content and examine the dehydroxylation of each clay within the study. The TGA analysis of each clay was additionally used to determine the most suitable calcination temperature. The oxide compositions were obtained by wavelength-dispersive X-ray fluorescence (WD-XRF) using the PANalytical AXIOS instrument (supplied locally via Malvern Panalytical Pty Ltd, Sydney, Australia) (Table 3).

**Table 3.** Oxide compositions analysed via XRF for various calcined clays.

| Phase | ICC | FCC | ACC | BCC | CCC | DCC |
|---|---|---|---|---|---|---|
| Amorphous (%) | 73.4 | 56.2 | 46.1 | 66.5 | 65.3 | 53.5 |
| Anatase (%) | 2.0 | - | - | - | - | - |
| Hematite (%) | 2.3 | 0.4 | - | 1.2 | - | - |
| Mullite (%) | 1.0 | 2.1 | - | - | | - |
| Quartz (%) | 15.2 | 20.3 | 17.1 | 2.6 | 24.7 | 14.2 |
| Illite (%) | - | - | 8.3 | - | 4.4 | - |
| Muscovite (%) | - | - | - | - | 9.3 | - |

### 2.1. Sample Preparation

The experimental procedure for the paste mixes involved nine different mix designs based on the ASTM C305 guidelines [26]. The details of each mix design can be found in Table 4, which outlines the composition and proportions used. To simplify the investigation and identify key factors related to individual calcined clay properties, the same GP cement replacement rate and water-to-cement ratio were used for all mixes.

**Table 4.** Mix design of the autogenous shrinkage pastes.

| Mix Name | Mix Design | Calcined Clay (g) | GP Cement (g) | Limestone (g) | FA (g) | Water (g) | Total (g) |
|---|---|---|---|---|---|---|---|
| GP | 100% GP Cement | - | 900 | - | - | 360 | 1260 |
| FA | 70% GP Cement/30% FA | - | 630 | - | 270 | 360 | 1260 |
| ICC | 70% GP Cement/10% Limestone/20% ICC | 180 | 630 | 90 | - | 360 | 1260 |
| FCC | 70% GP Cement/10% Limestone/20% FCC | 180 | 630 | 90 | - | 360 | 1260 |
| ACC | 70% GP Cement/10% Limestone/20% ACC | 180 | 630 | 90 | - | 360 | 1260 |
| BCC | 70% GP Cement/10% Limestone/20% BCC | 180 | 630 | 90 | - | 360 | 1260 |
| CCC | 70% GP Cement/10% Limestone/20% CCC | 180 | 630 | 90 | - | 360 | 1260 |
| DCC | 70% GP Cement/10% Limestone/20% DCC | 180 | 630 | 90 | - | 360 | 1260 |

Two reference mixes were developed: one mix containing 100% GP cement and another combining 70% GP cement with 30% FA. These reference mixes served as benchmarks for comparison purposes throughout the study.

Each of the six $LC^3$ blends consisted of 70% GP cement, 20% calcined clay, and 10% limestone by weight ratio. The water-to-binder ratio for all paste mixes was maintained at a value of 0.4 following ASTM C305 specifications [26]. Notably, gypsum was not added to any of the formulations due to the OPC already containing up to an acceptable level of 7.5%, which is an estimated 6.7% with the reduction of 30% removed from the mix.

The preparation of the pastes followed the procedures outlined in ASTM C305 [26]. Following procedures using a Hobart mixer (Hobart, Silverwater, Australia) operating at low and high speeds of 140 rpm and 285 rpm, the pastes, after being prepared and mixed, underwent several key analyses including isothermal calorimetry, autogenous shrinkage, XRD, XRF, and pore-size distribution measurements. To consistently maintain a stable experimentation temperature of 23 $\pm$ 2 °C, all paste material, along with containers and water experimentation, was placed in a temperature chamber set at 23 $\pm$ 2 °C with a controlled humidity of 50 $\pm$ 3% at least 24 h before casting. Once all the pastes were casted for micro-structural analysis, they were kept in the same temperature chamber until the day of testing.

### 2.2. Experimental Methods

#### 2.2.1. Calorimetry

To investigate the heat released by each calcined clay in the $LC^3$ mix design, isothermal calorimetry was performed using the Calmetrix I-Cal 4000 Isothermal Calorimeter (Calmetrix, Boston, MA, USA) instrument at UTS Tech Lab in Botany. The composition of the calorimetry paste mix followed the standard 30% $LC^3$ replacement design made up of 20% calcined clay and 10% limestone, with the rest consisting of OPC (70%). Gypsum

(retarder) was not included since high levels of GP indicated sufficient retardation. A total paste weight of 50 g was loaded into the Calmetrix I-Cal 4000 with a reference sample maintained at a temperature of 23 °C.

#### 2.2.2. Autogenous Shrinkage

Three replicates of each paste sample were cast into autogenous shrinkage moulds and were examined routinely to monitor the autogenous shrinkage, following the guidelines specified by ASTM C1698 [27]. The average of the three readings was calculated and used for the analysis. The preparation of the paste was carried out according to ASTM C305 [26] and filled into corrugated tubes as mentioned. To prevent any swelling caused by the re-absorption of bleed water, both ends of the tubes were sealed with caps and rotated in the rotation device shown in Figure 1. The rotation device and samples were kept within a temperature-controlled room at 23 ± 2 °C until 24 h after preparation as suggested by Mohr and Hood (2010) [28]. A horizontal gauge meter provided by Germann Instruments (Germann Instruments, Copenhagen, Denmark) was used to measure the autogenous shrinkage. The initial and final setting times for each mix were determined using the Vicat needle test in accordance with ASTM C191 [29]. These results are presented in Appendix A. The time axis ($t_0$) was aligned to the final setting time of each mix (where the *y* axis of each mix becomes horizontal), meaning that the first recorded data, where the plot becomes horizontal, corresponded to $t_0$ at the moment each mix reached its final setting time. After 24 h, the samples were removed from the rotation device, the measurement was recorded, and the samples were continually stored in a climate chamber set to a temperature of 23 ± 2 °C alongside paste samples for microstructural analysis.

**Figure 1.** Rotation device for the autogenous shrinkage samples for the first 24 h.

Initially, autogenous shrinkage was measured at regular intervals during the first week to closely monitor shrinkage behaviour. After that, the frequency of measurements was reduced when shrinkage stabilised.

#### 2.2.3. Chemical Shrinkage

The chemical shrinkage samples were prepared using a modified version of ASTM C1608 [30], as described by Zhang et al. (2013) [31]. Instead of small glass vials, an Erlenmeyer flask was used (Figure 2), and the thickness of the paste in the flask remained consistent at 8–10 mm for all samples. Pipettes were placed in the flash rubber lids to measure the difference in levels and then sealed all over with various glues to ensure airtight seals (Figure 2). Two replicates were made for each of the eight mixtures. Data

collection followed the ASTM C1608 [30] guidelines, with data being collected for up to 200 days. Chemical shrinkage measurements were monitored while a temperature of 23 ± 2 °C was maintained.

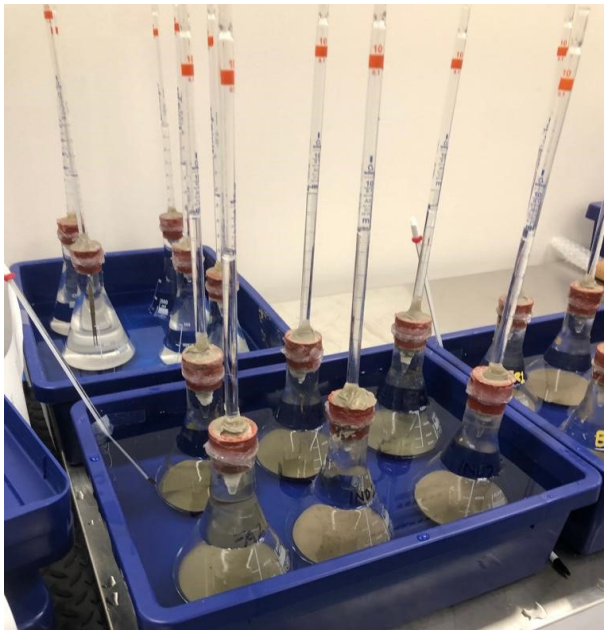

**Figure 2.** Chemical shrinkage Erlenmeyer flasks in water for temperature control.

#### 2.2.4. Microstructural Analysis

The microstructure analysis involved a comprehensive range of techniques, such as TGA, powder XRD, attenuated total reflection—FTIR—, and pore-size distribution measurements. The microstructural evaluation was divided into two parts: the first included time-dependent hydration analyses using XRD, TGA and FITR, with data collection at hydration periods of 1, 3, 7, 14, 28, 56, and 100 days from setting time; the second included the investigation of porosity by using nitrogen adsorption/desorption and the Barrett–Joyner–Halenda (BJH) method on hydrated paste samples at 1, 3, and 7 days.

To simplify the examination of the microstructural properties, ice cube moulds were used for casting. The eight binder paste mixtures were poured into these moulds and then securely sealed before being placed in a controlled environment with a temperature of 23 ± 2 °C until the designated day of testing. On the day of testing, the sides of the ice cubes were carefully removed using a mortar and pestle, allowing access to crush the inner core for analysis. After crushing, fragments from each sample were collected and passed through an 850 µm mesh sieve in preparation for examination of microstructural characteristics.

To halt the hydration process at specific testing intervals, a solvent-exchange technique utilising isopropanol was employed according to the method described by Snellings et al. (2018) [32]. The powdered sample was immersed in isopropanol with a mass ratio of 3 g of solid material per 100 mL of solvent. Afterwards, the samples were dried for 2 days using a vacuum oven at 40 °C. Subsequently, they were transferred into plastic vials and placed inside a sealed vacuum oven maintained at a temperature of 23 °C.

The hydration process at various testing intervals (1, 3, 7, 14, 28, 56, and 100 days) was assessed via TGA, XRD, and FTIR. The TGA analysis was analysed using the same TGA procedure outlined in Section 2.1. To conduct crystallographic analysis, powder XRD was carried out using the same equipment and parameters as those described in Section 2.1. The FTIR spectra were obtained using a Perkin Elmer Frontier IR spectrophotometer (PerkinElmer Inc, Waltham, MA, USA) equipped with a 3 mm diameter diamond/ZnSe crystal. Spectra were collected with a resolution of 2 $cm^{-1}$ and an accumulation

of 32 readings from 4000 $cm^{-1}$ to 400 $cm^{-1}$ per spectrum. Only the band between 550 $cm^{-1}$ and 2100 $cm^{-1}$ was considered for result analysis as it contained the reaction products.

Nitrogen adsorption isotherms were measured at 1-, 3-, and 7-day intervals to study the pore structure. The IQ absorb equipment at UTS Environmental Lab, Ultimo, was utilised for this purpose. The range of relative pressure (P/Po) covered from 0.005 to 0.995, encompassing a total of 82 points obtained from both adsorption and desorption processes. To analyse the pore structure effectively, the BJH method was used [33]. A thorough examination was carried out to compare the variations in pore-size distributions on different days to establish a relationship between pore-size distribution, chemical shrinkage, and autogenous shrinkage. To prepare for the isotherm collection process, a degassing procedure was employed which involved eliminating physically adsorbed water at a relatively low temperature of 40 °C over 16 h. This particular degassing protocol adhered closely to recommendations provided by Scrivener et al. (2016) and took place under vacuum conditions specifically for the pore-size distribution analysis [34].

## 3. Results

### *3.1. Isothermal Calorimetry*

Figure 3 presents the isothermal calorimetry results obtained on both the reference samples and those incorporating calcined clay material. The findings shown in Figure 3 indicate a faster acceleration of $LC^3$ after the induction phase. After the initial peak, a subsequent peak emerges, mirroring C3A in OPC. This initial peak is attributed to silicate phases (silicate peak), while the succeeding peak results from alumina derived from clinker or calcined clay [35]. As per Zunino and Scrivener (2019), this second peak arises from the hydration of aluminate phases in clinker [35]. Comparable peaks have been noted in studies involving lime-calcined clay–gypsum systems lacking aluminate phases. The presence of gypsum and kaolinite in the clay influences the positioning of this second peak, as illustrated in Figure 3. It was observed that for both GP and FA, the silicate peak (peak "1" in Figure 4a) appeared approximately 6 h after reacting with water. However, in the case of $LC^3$ mixtures, this silicate peak (peak "1") occurred earlier at around 4–5 h with a decrease in intensity compared to the reference mixes. This confirms that in the $LC^3$ system, there is an accelerated development of silicate peak formation [9].

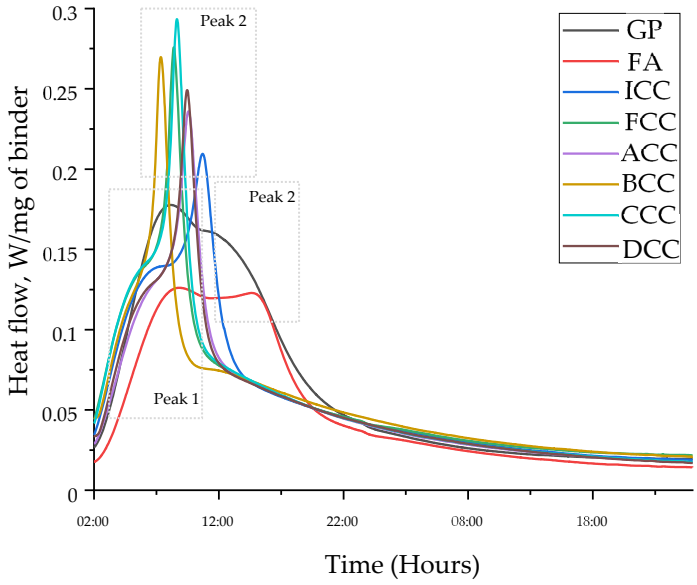


**Figure 3.** Heat evolution of all mixes indicating the silicate and alite peaks.

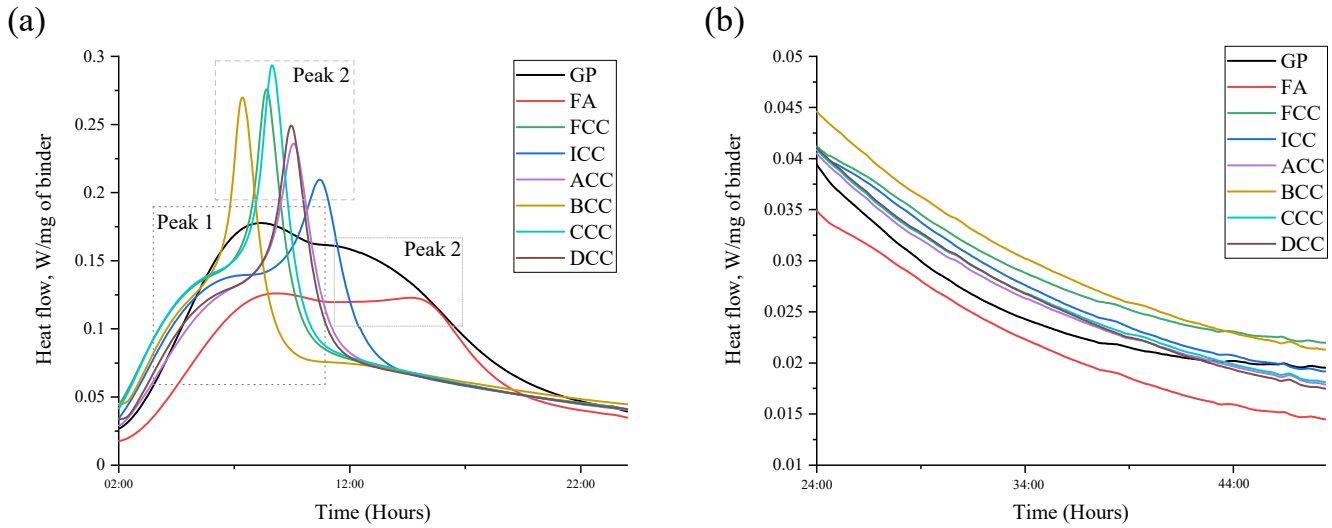


**Figure 4.** The heat of evolution. (**a**) First 24 h and (**b**) 24 to 38 h.

The presence of the silicate peak in the $LC^3$ mixes indicates that active hydration is occurring within the alite phase. The declining trend of peak "1" suggests that there is a decreasing proportion of clinker content in the $LC^3$ compositions, which is true as the $LC^3$ binder includes only 70% GP, and the rest is calcined clay and limestone. It has been observed that finer SCMs can enhance the reactivity of the alite phase, causing CCC, FCC and ICC samples to react first [36,37]. However, it is noticeable that BCC also forms one of the earlier alite peaks despite having a larger particle size compared to other $LC^3$ mixes.

After the silicate peak, another distinct peak (referred to as "peak 2") appears within the heat flow curve. This peak is caused by the reaction of aluminates after sulphate content depletion. As shown in Figure 4a, the intensity of the aluminate peaks increases with higher limestone amounts in $LC^3$ compositions compared those in GP cement and FA mixes, consistent with previous research findings. Mixtures containing fine limestone lead to an earlier onset and a steeper incline in the heat flow curve during the acceleration phase, which is known as the "filler effect" due to the fine limestone [37]. Additionally, Zunino and Scrivener's (2019) research is in line with this observation, shedding light on the heat released during the aluminate reaction and the formation of compounds such as ettringite [35]. Zunino and Scrivener (2019) indicated that systems incorporating metakaolin exhibit a higher heat output and also underscored metakaolin's role in these reactions, especially its contribution to the meta-kaolin content influencing the aluminate peak of the calcined clay mixes [35]. This was observed occurring in the $LC^3$ mixes (Figure 4b) where the depletion of sulphate contributed to the enhancement of aluminate peaks.

### *3.2. Autogenous Shrinkage*

The total autogenous shrinkage up to 200 days is shown in Figure 5, with the results showing that pastes containing FA present the lowest autogenous shrinkage at all times, which is consistent with Siddique and Khan's (2011) study [7]. This is attributed to FA's slow-releasing pozzolanic effect, which has been demonstrated in many studies, often leading to low strength during the early ages [38]. The other reference mix with 100% GP cement presented higher autogenous shrinkage than did the FA reference mix. However, from 25 days to 200 days, the autogenous shrinkage of the reference (100% GP) mix was less than that of all the $LC^3$ mixes. This is because from about 25 days, the increasing rate of autogenous shrinkage reduces significantly (almost plateaus), whereas the increasing rate of autogenous shrinkage of $LC^3$ mixes remains high until about 50 days and then gradually reduces. For this reason, from 25 days, all $LC^3$ mixes underwent higher autogenous

shrinkage. The calcined clays in this study were processed in similar natures but were vastly different from each other in terms of physical and chemical properties.

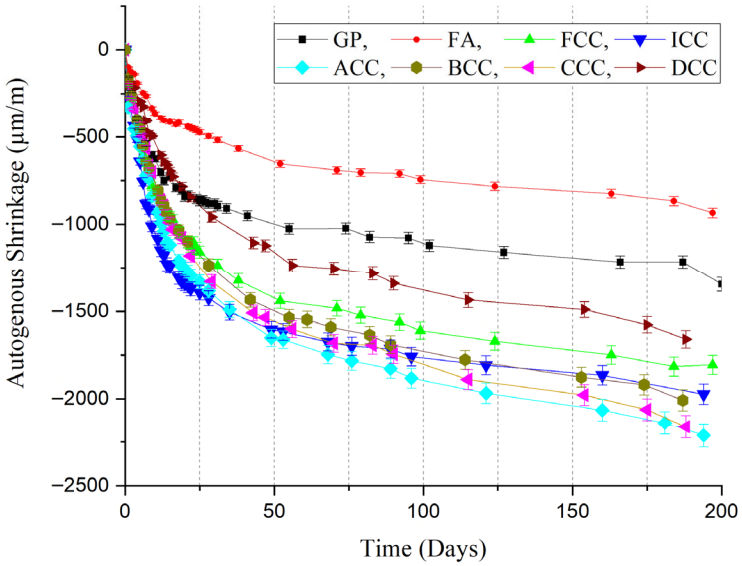


**Figure 5.** Total autogenous shrinkage of all mixes.

Mix DCC, which has low kaolinite content, a reasonable amorphous content, and large particle size distribution, exhibited significantly lower autogenous shrinkage when compared to the other $LC^3$ mixes. On the other hand, ACC and CCC mixes displayed the highest overall autogenous shrinkage. These two calcined clays had smaller particle sizes and larger surface areas than did the DCC mix. The reduced autogenous shrinkage observed in the DCC mix can be attributed to its unique composition characteristics. In contrast, ACC and CCC mix, having finer particles, tend to have increased water demand during mixing due to their larger surface area per unit volume of cementitious material incorporated into the paste matrix. As a result, they both exhibited greater internal self-desiccation leading to higher autogenous shrinkage over time. For the first 25 days, all $LC^3$ mixes underwent high autogenous shrinkage and then continued shrinking at a much slower pace. However, after 90 days, the $LC^3$ mixes underwent autogenous shrinkage similar to that of the reference GP and FA mixes. The main reason causing autogenous shrinkage was self-desiccation, which occurred in the samples where the condition included no external moisture during hydration. Therefore, the factors needed to gain a comprehensive overview of autogenous shrinkage in $LC^3$ systems are (1) hydration products, (2) rate of hydration, and (3) pore structure.

Figure 6 exhibits the autogenous shrinkage of the eight mixes in the first 7 days. FA showed the lowest levels of autogenous shrinkage. The $LC^3$ mixes presented a rapid autogenous shrinkage development but were relatively similar to the reference GP mix except for ICC and ACC, which both achieved higher shrinkage compared to the GP reference mix. This could be due to the higher kaolinite content that is associated with ACC. $LC^3$ mixes accelerating in shrinkage is common within the first 24 h due to the increased surface area and activation of the pozzolanic reaction. In the comparison of the Australian $LC^3$ blends, it is evident that their early-age autogenous shrinkage follows a trend based on kaolinite content and surface area. ACC specimens underwent higher autogenous shrinkage compared to other Australian $LC^3$ mixtures, while DCC underwent lower shrinkage. Unfortunately, ICC and FCC were calcined before delivery and hence could not be included in this trend examination; however, the surface area of the two reference calcined clays is consistent with this evaluation. DCC demonstrated a rapid

increase in shrinkage during the first day of hydration, however, slowed down thereafter, achieving less autogenous shrinkage than GP for the first 7 days. This demonstrates a further need to explore the calcined clays being used in $LC^3$ mixes and to understand the shrinkage properties in greater depth.

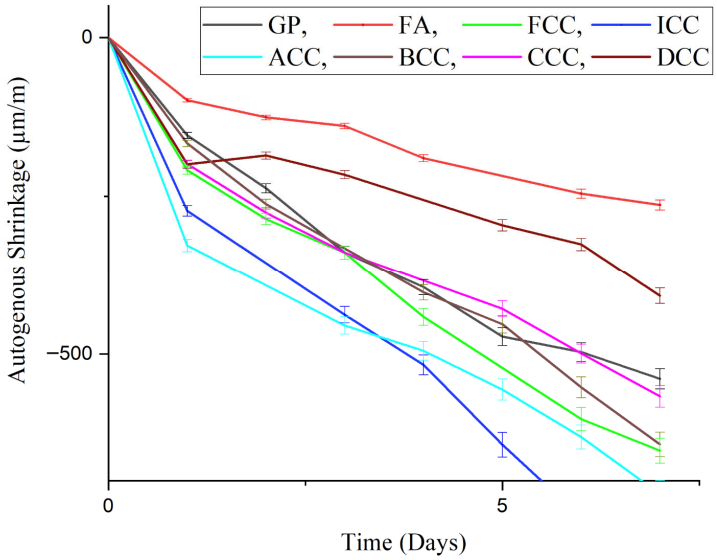


**Figure 6.** Autogenous shrinkage of all mixes up to 7 days.

### *3.3. Chemical Shrinkage*

Chemical shrinkage is the reduction in the volume of cement pastes upon undergoing constant hydration, attributed to the decreased volume of the resultant products relative to the initial reactants; the pastes remaining fully saturated in this form, which allows for the effect of self-desiccation to be minimised [39]. This phenomenon helps determine the earliest stages of deformation in cement paste immediately after amalgamation. Figure 7 shows similar overall trends for all pastes. Noticeably FA shows the lowest chemical shrinkage as it initially serves as a filler, reducing shrinkage significantly in early-stage hydration (Figure 7), which also aligns with other researchers' findings [17,40]. However, DCC acts in a similar fashion to FA, demonstrating the same trend and similar shrinkage results.

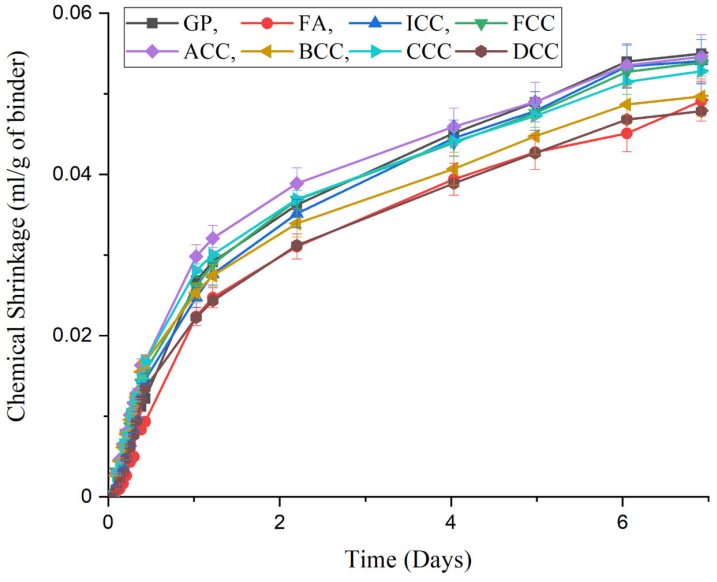


**Figure 7.** Chemical shrinkage for all mixes up to 7 days.

Figure 8 illustrates the measurements for total shrinkage up to 200 days. It is worth noting that the control GP mix reaches a plateau between 30 and 60 days and then has very minor movements between day 90 and day 100, which may be caused by a minor disturbance in the environment (a bump, temperature change). All $LC^3$ mixes exhibit lower chemical shrinkage than does GP throughout the measurement period. At 7 days, every $LC^3$ blend shows reduced chemical shrinkage relative to GP, with DCC (−13.0%) and BCC (−9.6%) demonstrating the greatest early-age reductions; FA also shows lower shrinkage than does GP (−10.7%) at this stage due to its delayed pozzolanic activity. At 28 days, this trend persists, with $LC^3$ reductions ranging from −2.0% to −14.8% (again highest for DCC and BCC), while FA remains only marginally below GP (−2.9%). By ~100 days, where the curves stabilise and an apparent equilibrium is reached, FA increases to +11.5% above GP, whereas all $LC^3$ systems remain below GP (approximately −1% to −10%), with BCC and DCC achieving the largest long-term reductions.

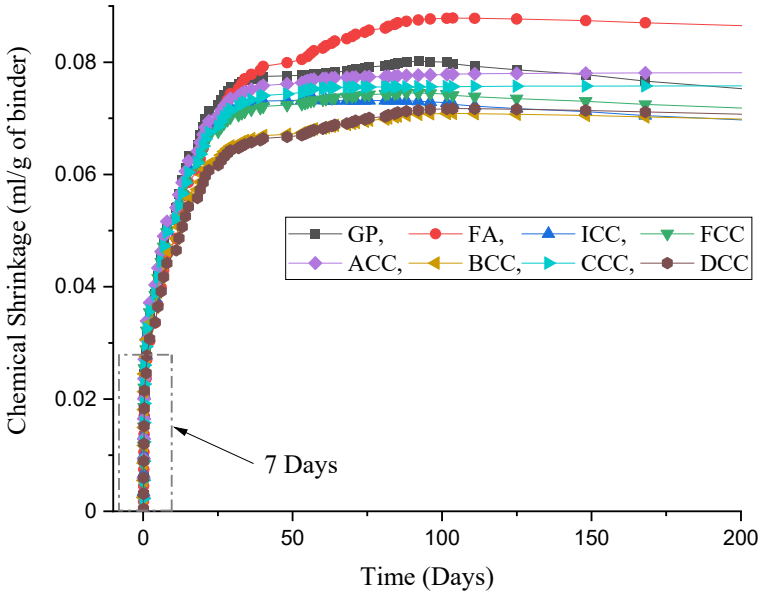


**Figure 8.** Total chemical shrinkage of all mixes up to 200 days.

All $LC^3$ mixes exhibited a lower level of chemical shrinkage compared to the reference mixes. This can be attributed to several factors unique to $LC^3$ blends. Calcined clay is a natural pozzolan with high reactivity, which when hydrating, effectively reduces the amount of portlandite available for the hydration reactions that contribute to chemical shrinkage. A previous study showed that the use of limestone filler in concrete mixtures also helps suppress chemical shrinkage by providing smaller particle sizes and increased surface area for hydration reactions [36]. BCC and DCC reached complete shrinkage stabilisation by 100 days, consistent with their lower surface areas compared to other $LC^3$ blends, while the remaining $LC^3$ mixes reached plateaus similar to the GP reference. The combination of calcined clay and limestone in the $LC^3$ mixes resulted in low total chemical shrinkage when compared to the reference materials of GP and FA. Although $LC^3$ mixes minimised chemical shrinkage relative to GP and FA, they exhibited greater autogenous shrinkage. This behaviour is consistent with the self-desiccation caused by their refined pore structures, indicating that increased matrix densification, while beneficial for reducing chemical shrinkage, also contributes to higher internal water consumption and autogenous deformation.

### *3.4. Microstructural Analysis*

TGA was utilised to monitor the hydration progress of the six $LC^3$ mixtures. This analysis involved conducting measurements at specific intervals—1, 3, 7, 14, 28, 56, and 100 days. The objective behind examination via TGA was to thoroughly analyse and interpret how the different calcined clay mixes hydrate and to gain a comprehensive understanding of the variation between $LC^3$ mixtures as well as its impact on shrinkage.

The TGA and DTA results of the $LC^3$ hydrated pastes monitored at 1, 3, 7, 14, 28, 56, and 100 days are presented in Figures 9 and 10. The TGA weight loss is progressive in all mixes due to the thermal decomposition of the pastes. All TGA results demonstrate a large weight drop between the first and third day, which indicates active hydration between these days, which aligns with the trends of the autogenous shrinkage between the first and third days. From then onwards, the hydration of the pastes seems relatively consistent, increasing along with time. Compared to findings reported by Afroz et al. [41], the GP reference mass difference increased rapidly between 1 and 14 days; however, in the case of the $LC^3$ mixes, the greatest mass differences were between 1 and 7 days, which also aligns with Afroz et al.'s (2021) [14] findings.

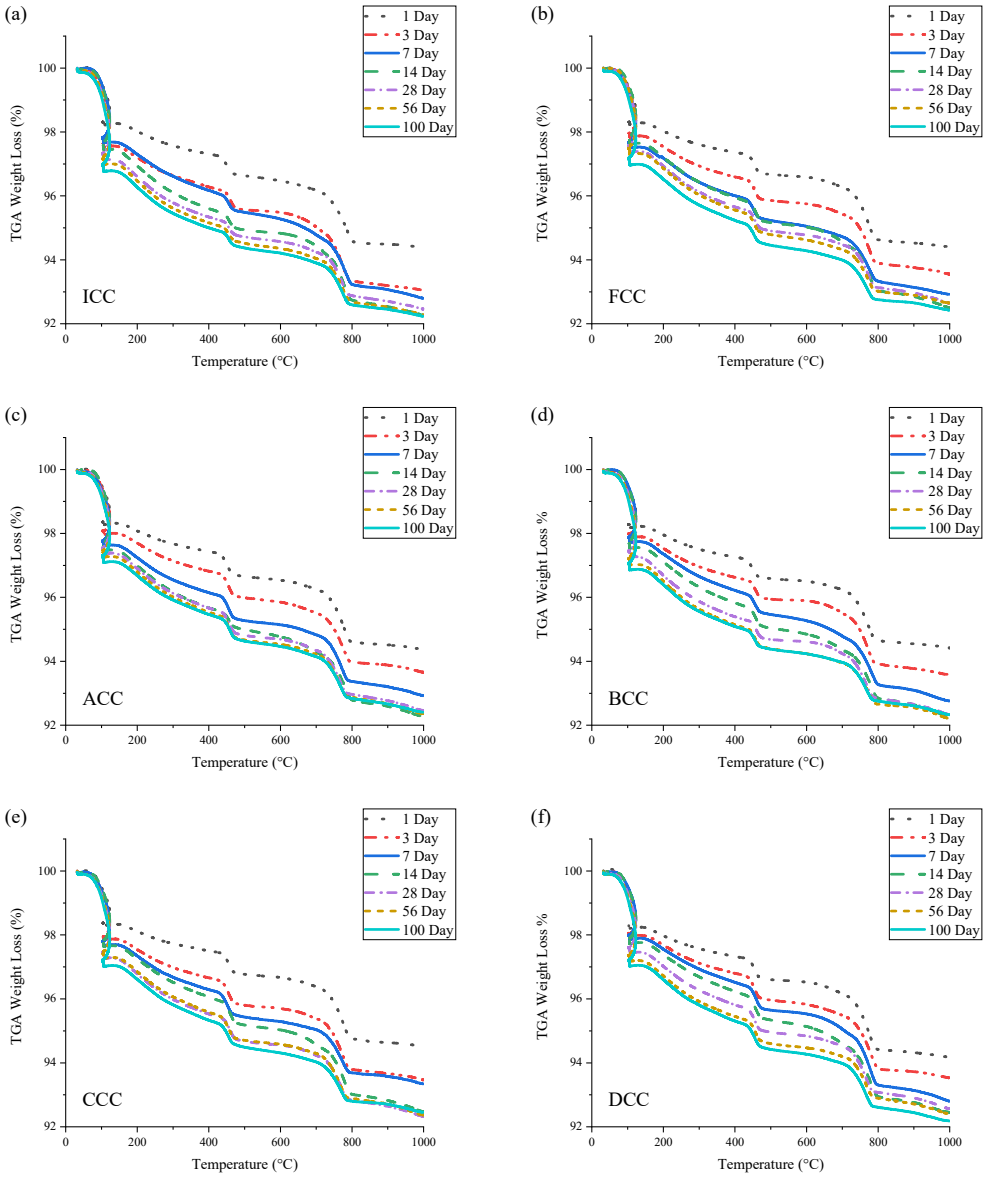


**Figure 9.** TGA weight loss of (**a**) ICC, (**b**) FCC, (**c**) ACC, (**d**) BCC, (**e**) CCC, and (**f**) DCC.

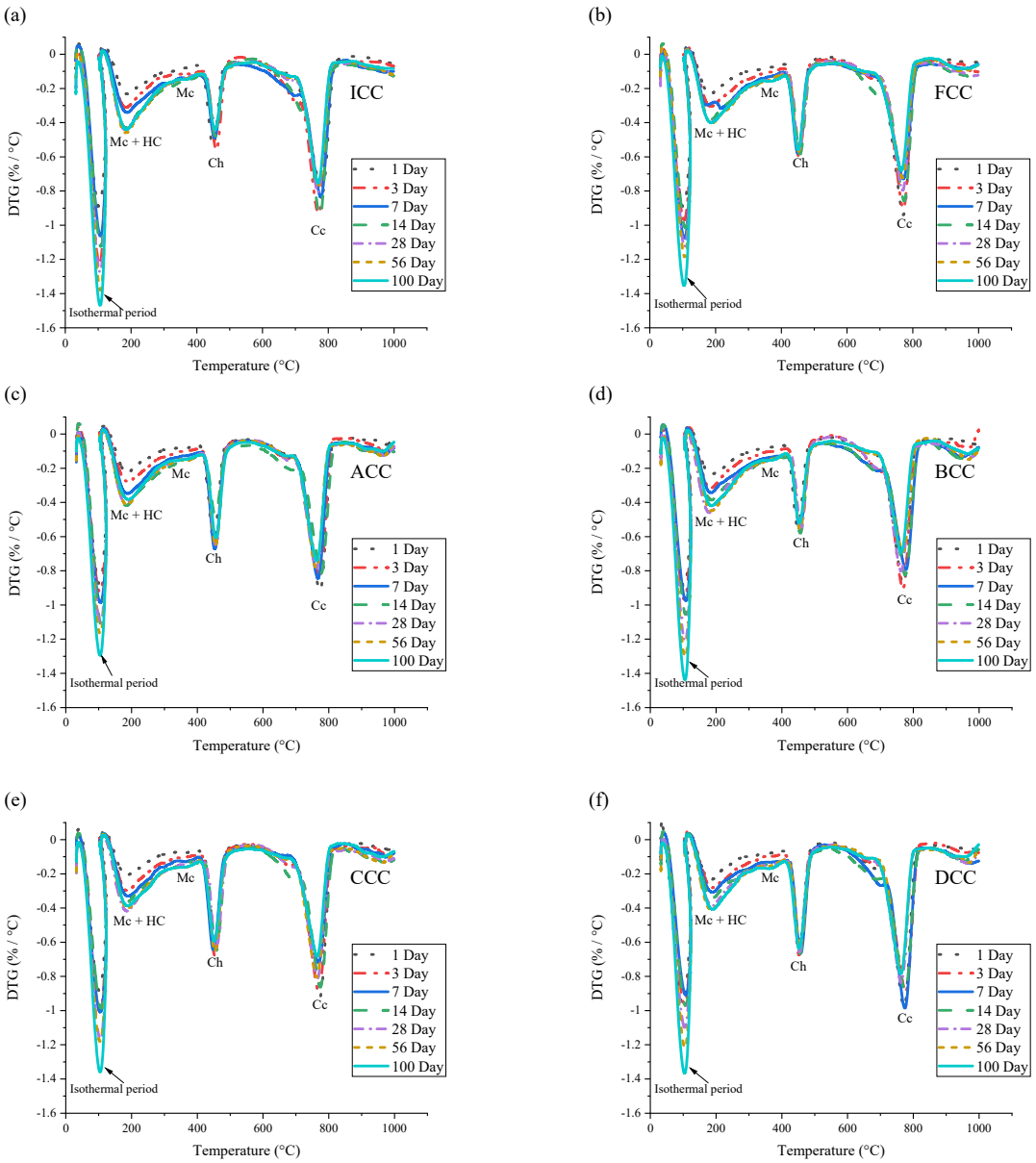


**Figure 10.** Differential TGA weight loss of (**a**) ICC, (**b**) FCC, (**c**) ACC, (**d**) BCC, (**e**) CCC, and (**f**) DCC.

In terms of the DTA (Figure 10), the peak at 105 °C indicates an isothermal process for the 30 min duration (Figure 10), which eliminates the solvent that was used (osopropyl) and frees water from the samples [32]. In the DTA analysis of $LC^3$ mixtures shown in Figure 10, a broad peak can be observed spanning from 140 °C to 190 °C. This indicates the presence of AFm (alumina, ferric oxide, monosubstituted) phases, specifically monocarboaluminate and hemicarboaluminate, overlapping with C-S-H, starting from day 14 for all $LC^3$ mixes. A distinct peak at around 160 °C is apparent, along with a smaller secondary peak at approximately 250 °C. These peaks can be attributed to the formation of monocarboaluminates. These findings align with previous research conducted by various researchers, which also reported on similar temperature ranges for monocarboaluminates [9,17,42].

The DTA results correspond closely to the autogenous shrinkage observed in $LC^3$ pastes. In the early stages (1–7 days) of hydration, there are notable differences in reactions among various $LC^3$ mixes. However, between days 7 and 56, these differences become less pronounced. Subsequently, from days 56 to 100, the changes observed in the hydrated pastes exhibit similarities, indicating a more consistent behaviour, which aligns with the autogenous shrinkage plateauing after 50 days.

Subsequent discernible mass drops occurred on every $LC^3$ mix (Figure 10) between 400 °C and 470 °C. This corresponds to the decomposition of calcium hydroxide (CH). All $LC^3$ mixes demonstrate weight loss within the range of 400 °C to 470 °C, which is linked to the pozzolanic impact of calcined clay. Interestingly each mix undergoes the greatest drop at different times, however, all within the early ages of hydration (1–7 days of hydration). This may have occurred due to the some of the pozzolanic material reacting in the later stages of the process. It should be noted that the mineralogy of calcined clays contains various components, including a relatively low amount of meta-kaolin in some of the calcined clays (BCC, CCC & DCC). The weight loss observed between the temperatures ranging from 470 °C to 790 °C indicates decomposition of calcium carbonate, with unreacted calcium carbonates found in all $LC^3$ samples. Similar to the decomposition behaviour observed for calcium hydroxide, all $LC^3$ mixes show a significant drop during the initial stages of hydration and then undergo a decrease over time, reaching their minimum value at 100 days (Figure 10).

#### 3.4.1. XRD Analysis

XRD analysis was performed to examine the phase composition of all $LC^3$ mixes in different hydrated paste samples with diverse mineralogical components, meta-kaolin content, and amorphous content. The assessment covered a range of time intervals spanning from 1 to 100 days. This comprehensive evaluation allowed for a thorough understanding of the evolution and development of mineral phases over time and their effects on shrinkage. The hydrated samples contained several primary crystalline phases, including ettringite, monocarboaluminate, hemicarboaluminate, calcite, and portlandite. These phases are shown in Figure 11. Additionally, other components such as quartz, calcium carbonate, and microline were found in trace amounts due to their presence in the raw materials before calcination as seen in Investigating Australian Calcined Clays as Supplementary Cementitious Materials [24]. It is worth mentioning that there was little variation observed in the phase assemblage among all $LC^3$ mixtures studied, with the main differences lying in the intensity of these phases during the hydration process.

The time-dependent XRD analysis indicated the formation of ettringite from day 1 in all $LC^3$ mixes. The intensity of ettringite peaks remained consistent up to 100 days, with the highest intensity at day 1 of hydration. The absence of monosulfoaluminate in XRD patterns could be attributed to either the presence of calcite or its concentration falling below the detection threshold of XRD due to its semi-crystalline nature [43]. Hemicarboaluminates were detected in all samples at all ages. However, there were inconsistencies observed when the time-dependent samples were compared to each other.

The intensities of hemicarboaluminates showed their highest peaks during the early stages, but not at day 1. All $LC^3$ samples exhibited more intense hemicarboaluminate peaks between days 3 and 14, which suggests late reactions involving these compounds. The delayed appearance of prominent hemicarboaluminate peaks in the $LC^3$ cement confirms its enhanced reactivity due to the reactive clays (illite, mullite, kaolinite) present in its composition. Minor monocarboaluminate peaks were initially detected on the first day of hydration in all $LC^3$ hydrated mixes; however, it was observed that BCC samples (Figure 11d) exhibited higher and more intense peaks compared to other $LC^3$ mixes. As time progressed, the intensity of monocarboaluminate peaks increased for all $LC^3$ samples. Interestingly, there were cases such as FCC and DCC (Figure 11b,f) where the peak with the highest intensity was observed at 56 days instead of 100 days. This indicates that the formation and development of monocarboaluminate is a complex process influenced by various factors including the calcined clay properties.

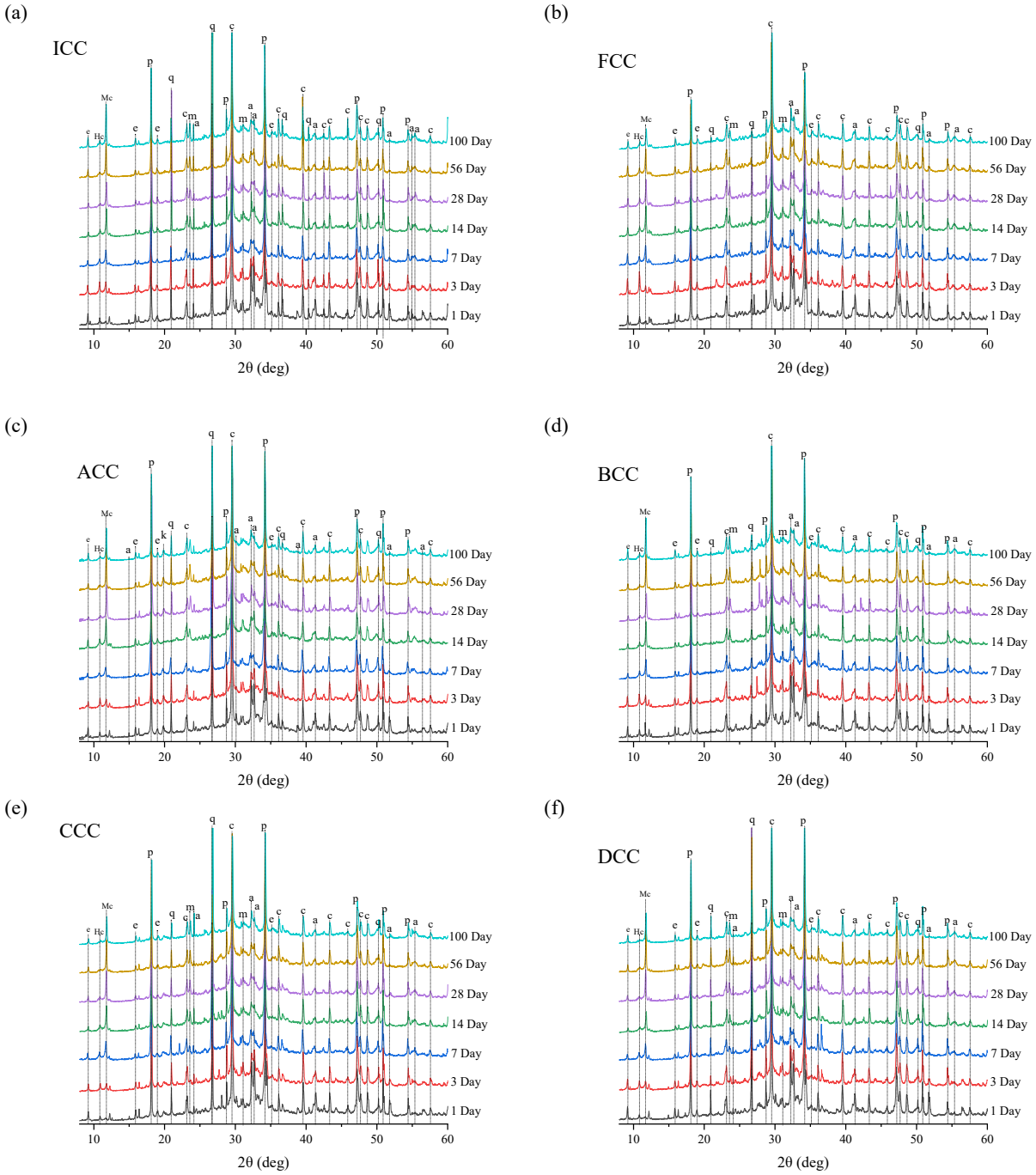


**Figure 11.** XRD phases present in hydrated paste sample at 1, 3, 7, 14, 28, 56, and 100 days. (**a**) ICC, (**b**) FCC, (**c**) ACC, (**d**) BCC, (**e**) CCC, and (**f**) DCC. (a = alite, c = calcite, e = ettringite, Hc = hemicarboaluminate, m = microline. Mc = monocarboaluminate, p = portlandite, q = quartz).

Based on the XRD results, as previously outlined in Investigating Australian Calcined Clays as Supplementary Cementitious Materials [24], it was observed that the phases identified before calcination remained consistent in the hydrated samples. The hydration process leads to the formation of various compounds, such as monocarboaluminate and hemicarboaluminate, as mentioned in previous studies. These compounds play a significant role in determining the properties and performance of $LC^3$ such as strength development, shrinkage, and setting times. Monocarboaluminate and hemicarboaluminate are phases associated with the early strength development of concrete and hydration, which in turn impact setting times and shrinkage [44].

3.4.2. FTIR Analysis

In Figure 12, the FTIR spectra of all $LC^3$ hydrated samples at various time points (1, 3, 7, 14, 28, 56, and 100 days) are presented. The obtained FTIR peaks are provided in Figure 12. Among these peaks, two distinct peaks were identified at wavenumbers of approximately 3853 $cm^{-1}$ and around 3739 $cm^{-1}$. These significant peaks are attributed to the presence of water molecules or hydroxyl groups within the sample. This observation suggests that these $OH^-$ groups may be linked to the solvent-exchange method employed during the hydration process [44].

The presence of a second peak at 2360 $cm^{-1}$ was identified in all samples during the first day, except for in FCC (Figure 12b) where it was not observed at all. This peculiar phenomenon may be attributed to the formation of an unknown specific reaction product. It is worth noting that this occurrence was limited only to the first-day samples and disappeared abruptly after one day. The disappearance of this peak suggests that the reaction associated with its formation reaches completion before reaching the third day.

The peak at 1520 $cm^{-1}$ in the spectrum obtained can be attributed to the stretching vibration of the O-C-O functional group, which is directly related to calcite [44]. This corresponds well with the XRD phases identified. Another peak observed at 1416 $cm^{-1}$ was associated with aluminosilicate vibrations and silicate vibrations. This can be indicative of C-A-S-H (calcium aluminate silicate hydrate) formation as reported by [45]. Additionally, another significant peak observed in this study was found at 953 $cm^{-1}$, which has been linked to C-S-H formation [46,47].

3.4.3. Pore-Size Distribution

The autogenous shrinkage of cement-based materials is strongly influenced by the distribution of pore sizes. The stresses occurring during shrinkage due to self-desiccation are unique to each size of pores, as water consumption takes place within them. In addition, the interconnection of these pores determines how moisture moves from saturated to unsaturated areas, which directly impacts the overall progression of the shrinking process [45–47]. The classification of pores introduced by Mindess et al. (1981) [48] provides a systematic framework for categorising different pore sizes. There are three classifications provided to differentiate between three main categories of pores: (1) small capillary pores, which are "gel" pores that have dimensions ranging from 1.25 to 5 nm and play a crucial role in retaining water within the material; (2) medium capillary pores, which have sizes ranging from 5 to 25 nm and significantly contribute to the overall capillary pore structure; and (3) large capillary pores, which encompass range of sizes from 25 nm up to 5 µm and have notable effects on both material strength and permeability.

It has been found that the size distribution of desorption pores relates to autogenous shrinkage because it directly affects the release of water during drying and hydration processes [49]. This mechanism closely relates to the phenomenon of autogenous shrinkage, where volume reduction occurs as water is consumed by hydration reactions. Smaller pores are especially significant in this process, as they have a higher tendency to release water, which greatly influences the magnitude of autogenous shrinkage [49,50]. Figure 13 illustrates the desorption behaviour of all $LC^3$ mixes at 1, 3, and 7 days. With the exception of ICC (Figure 13a), the majority of samples follow a common trend: the highest pore volume is observed at 1 day, followed by 3 days, and then 7 days.

In all samples (Figure 13), a consistent pattern emerges with two distinct peaks—the initial one within the gel pore range, followed by the second in the medium capillary pore region. This dual-peak trend is commonly observed in cementitious pastes. In the examination of the behaviour of Australian calcined clays (ACC (Figure 13c), BCC (Figure 13d), CCC (Figure 13e), DCC (Figure 13f)), certain trends become evident. ACC

(Figure 13c) and CCC (Figure 13e) exhibit similarities in the trends observed over 1, 3, and 7 days, with a notable gap between day 1 and day 3. Conversely, BCC (Figure 13d) and DCC (Figure 13e) demonstrate a shared pattern, characterised by a relatively smaller gap between day 1 and day 3, followed by a more significant gap between day 3 and day 7.

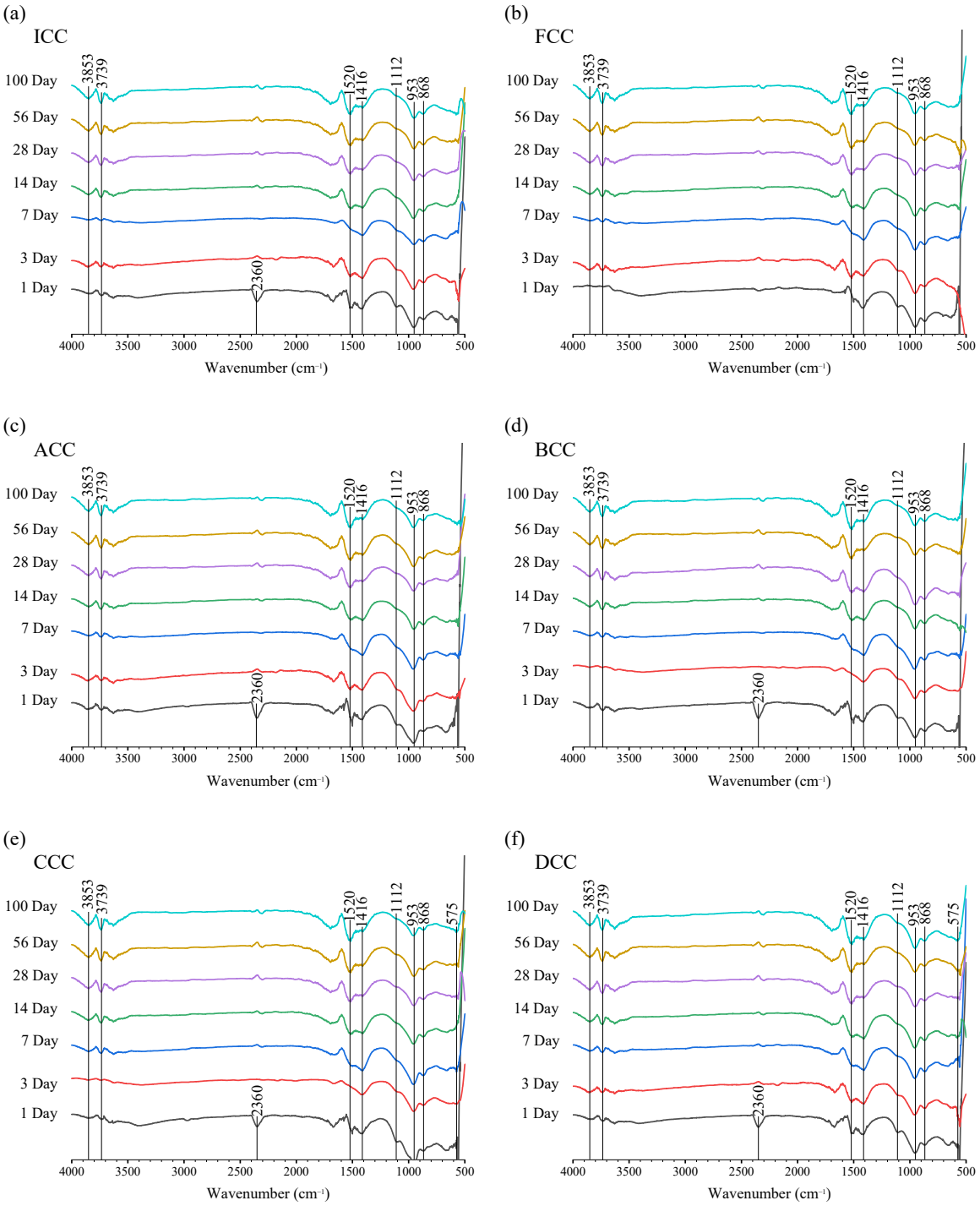


**Figure 12.** FTIR hydrated paste samples at 1, 3, 7, 14, 28, 56, and 100 days. (**a**) ICC, (**b**) FCC, (**c**) ACC, (**d**) BCC, (**e**) CCC, and (**f**) DCC.

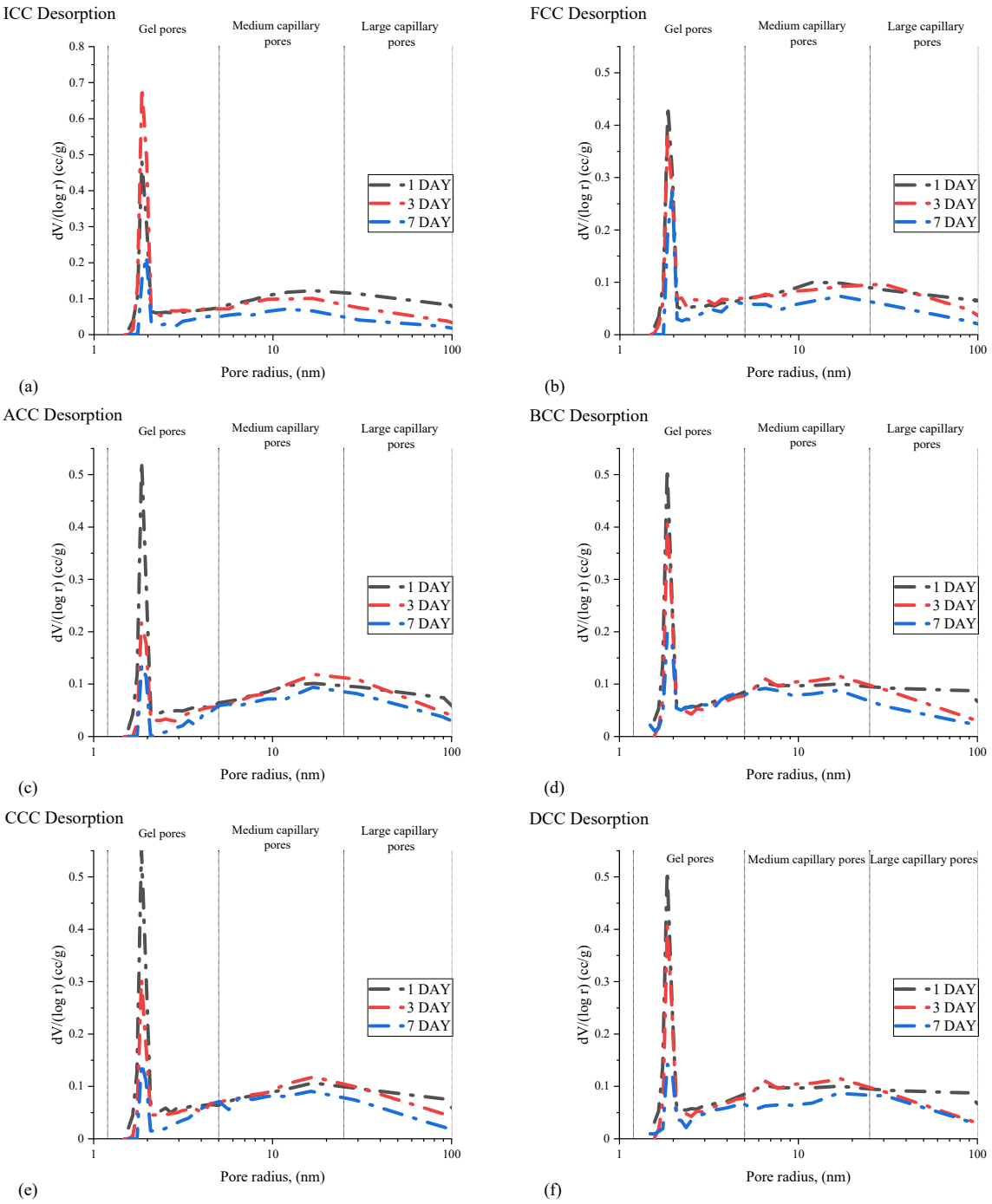


**Figure 13.** Different desorption pore-size distributions of hydrated paste samples at 1, 3, and 7 days. (**a**) ICC, (**b**) FCC, (**c**) ACC, (**d**) BCC, (**e**) CCC, and (**f**) DCC.

From related research that used a similar methodology to that used in our study, it was discovered that the GP mixture underwent a gradual development of finer pores, suggesting a gradual densification of the material. Between days 7 and 56, the cumulative pore volume for all pore sizes decreased. From days 56 to 90, there was a reduction in pore volume for pores larger than 11 nm, and larger pores were subdivided into smaller ones, leading to an increase in cumulative pore volume below 5 nm [41].

The reduced particle size of calcined clay and limestone can impact particle packing and therefore impact the shrinkage properties of the hydrated paste [39]. Conversely, the pozzolanic properties of calcined clay exert a more pronounced influence on pore-size reduction compared to its fineness, as supported by a previous study [51].

Analysing the trends presented in Figure 14 reveals distinct behaviours among the samples. One notable observation is that ICC demonstrates larger capillary pores on days 1 and 3 compared to other samples (Figure 14a). However, at day 7, these pore sizes decrease, indicating a shift towards smaller capillary pores. It is interesting to note that there are no consistent linear trends in cumulative pore volume. Nevertheless, it is worth mentioning that certain trends seem to correspond with the specific patterns of autogenous shrinkage observed in each mix. For example, ACC consistently maintains smaller capillary pore volumes throughout the testing period, which can be attributed to the highest autogenous shrinkage of ACC paste, as seen in Figure 5. These findings highlight how variations in capillary pore size distribution can greatly impact hydration properties such as autogenous shrinkage.

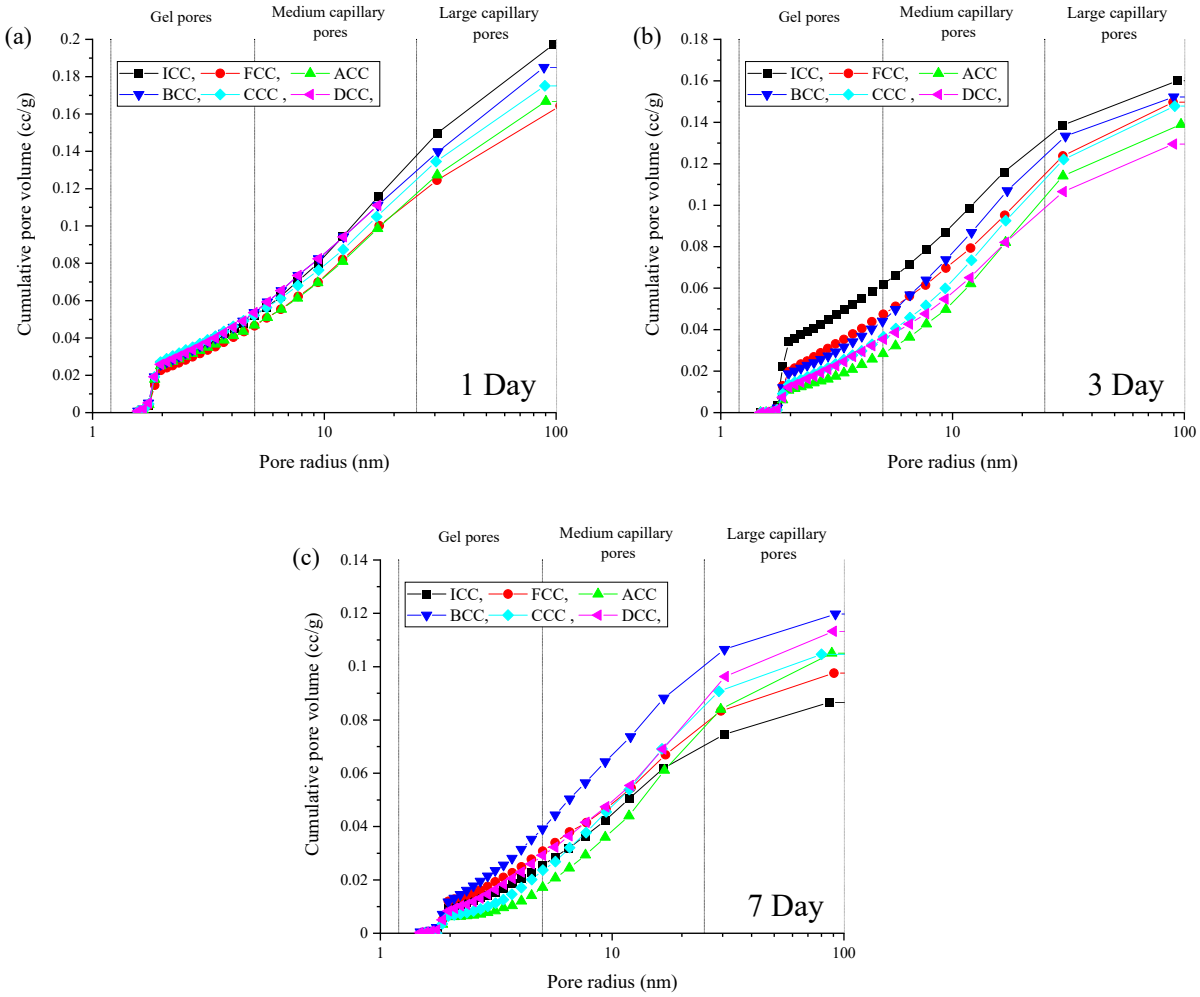


**Figure 14.** Different desorption pore-size distribution of hydrated paste samples at 1, 3, and 7 days.

## 4. Discussion

### *4.1. Chemical Shrinkage*

Upon analysis of the results presented in Figures 7 and 8, it becomes evident that all $LC^3$ mixes exhibited lower levels of chemical shrinkage compared to reference mixes GP cement and FA. This is due to the pozzolanic reaction of the calcined clay, leading to the densification of the cementitious matrix by reducing large pores. This densification effectively limits the material's capacity to shrink, resulting in low chemical shrinkage. These findings align with previous studies [12,52].

The presence of limestone filler in the $LC^3$ blends, in contrast to the OPC and FA blends, contributes to the reduction of chemical shrinkage and the acceleration effect demonstrated in the calorimetry of the pastes. Limestone filler provides smaller particle sizes and increased surface area for hydration reactions, which help counteract the volume reduction associated with chemical reactions, which has been observed in the research conducted by Bouasker et al. (2008) [39]. The combination of calcined clay and limestone in $LC^3$ binder systems resulted in lower chemical shrinkage compared to traditional cementitious materials.

The FTIR indicated the formation of calcite and C-S-H during hydration, which in turn contributed to the overall volume changes and reactions taking place within the material, which led to a reduction in chemical shrinkage by filling internal voids and limiting self-desiccation.

### *4.2. Autogenous Shrinkage*

The autogenous shrinkage development of $LC^3$ blends compared to that of the reference GP and FA mixes was significantly different, as shown in Figure 5. All $LC^3$ samples tended to exhibit higher autogenous shrinkage than did the references, but one, DCC, had an autogenous shrinkage similar to the trend of GP. After 56 days, FCC began to plateau before all $LC^3$ blends. One of the contributing factors that is associated with DCC's low autogenous shrinkage is less pozzolanic reactions due to the low kaolinitic content of the clay (30.95%). The finding suggests an advantage in the ability to control the mechanical properties of concrete by selecting a particular type of clay (with less kaolinite content) depending on the requirements of the structure. The advantage of this study and the analysis of various clays in the experiments is in providing a greater understanding of which properties of the clay affect what to determine the outcome for future use.

Figure 15 shows a noticeable correlation between autogenous shrinkage and pore volume across the first 7 days of autogenous shrinkage, with an average $R^2$ value of 0.96. This indicates that the pore volume has a direct correspondence to the autogenous shrinkage. These findings are consistent with previous research by Afroz et al. (2023) [17], Nguyen et al. (2022) [11], and Yodsudjai and Wang (2013) [53], which also demonstrated similar trends in autogenous shrinkage behaviour. The $R^2$ results align with those of Afroz et al. (2023) [17] and Nguyen et al. (2022) [11], which also demonstrate similar $R^2$ findings. The consistency across these studies underscores the well-recognized influence of structure refinement on material behaviour, specifically that related to autogenous shrinkage due to the effect of self-desiccation.

The accelerated hydration observed in some $LC^3$ blends seems to lead to higher autogenous shrinkage, specifically at the early age (1–7 days), as displayed in Figure 6; however, as mentioned earlier, DCC is an exception, and underwent less autogenous shrinkage than did GP within the early ages (1–7 days). The autogenous shrinkage is also linked to its silicate and alumina phases identified during the calorimetry testing, as outlined in Section 3.1. The declining trend of the silicate peak ("peak 1") suggests a reduction in the availability of clinker content in $LC^3$ compositions, as all $LC^3$ mixes underwent a high peak followed by a sharp downward trend, unlike the reference mixes which displayed more of a hump. As the silicate peak is sharp in Figure 3, this indicates fast water consumption of the $LC^3$ mixes, which in turn leads to high rates of autogenous shrinkage. The appearance of the alumina peaks ("peak 2") in the heat flow curve, with increased intensity in $LC^3$ compositions that contain higher limestone amounts than the references, underscores the enhanced reactivity of the aluminate phases. This reactivity shift directly influences the formation of hydration products and their associated volume changes. Given that autogenous shrinkage is driven by the loss of water during hydration

and is self-desiccating, the changes in the reactivity of specific phases contribute to the overall water consumption and subsequent volume changes during the early stages of hydration. The kinetics of the reaction and the quantity of reaction product are important; however, after the early stages of hydration, there is limited to no chemical shrinkage, which in turn means there are no more hydrates in the system (at least not involving shrinkage). Therefore, the main parameter affecting autogenous shrinkage after the early ages of hydration is the pore structure.

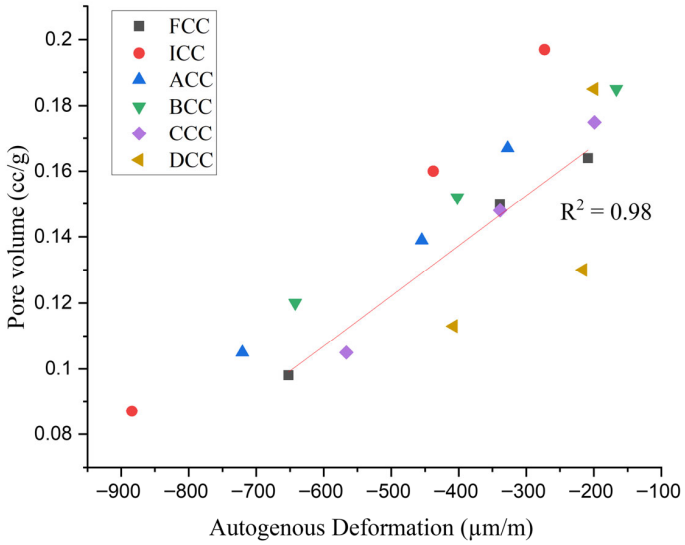


**Figure 15.** A linear relationship between autogenous deformation and pore volume across 7 days.

In the context of autogenous shrinkage, the alterations in thermal behaviour and hydration kinetics provide a nuanced understanding of the underlying mechanisms influencing this phenomenon. The accelerated hydration, changes in the availability of reactants, and shifts in phase reactivity collectively contribute to the intricate relationship between water consumption and volume changes.

## 5. Conclusions

This study evaluated the chemical and autogenous shrinkage of $LC^3$ pastes compared with that of GP and FA systems. Based on the experimental results, the main conclusions are as follows:

- $LC^3$ blends showed the lowest chemical shrinkage among all mixes tested. This is attributed to the filler effect of limestone and the accelerated early hydration resulting in a denser microstructure, especially with mix BCC and DCC.
- $LC^3$ blends exhibited higher autogenous shrinkage compared to reference materials, which was influenced by the characteristics of the calcined clay used. High reactivity metakaolin (ACC) and finer particles with larger surface areas tend to result in increased water demand during mixing, higher internal self-desiccation, and higher autogenous shrinkage over time.
- $LC^3$ pastes exhibited a refined pore structure, and a strong correlation was observed between pore refinement and autogenous shrinkage, particularly during the first 7 days.
- XRD and FTIR confirmed the formation of ettringite, monocarboaluminate, and hemicarboaluminate during hydration. After 28 days, monocarboaluminate remained stable, contributing to the longer-term dimensional stability in $LC^3$ mixes.

In summary, the study highlights the complex interplay between material properties, phase evolution, pore characteristics, and shrinkage in $LC^3$ pastes. The results emphasise

the need for a comprehensive understanding of these factors to develop more sustainable and effective cementitious materials for construction applications.

**Author Contributions:** Conception, A.C.; methodology, E.C., A.C. and R.S.N.; formal analysis, E.C., A.C., R.S.N. and H.R.; writing—original draft, E.C., A.C., R.S.N. and H.R.; supervision, A.C., R.S.N. and H.R.; funding acquisition, A.C. All authors have read and agreed to the published version of the manuscript.

**Funding:** This research received no external funding.

**Data Availability Statement:** The data that support the findings of this study are available from the corresponding author upon reasonable request.

**Acknowledgments:** The authors would like to thank the UTS Boral Sustainability Centre and the School of Civil and Environmental Engineering, University of Technology Sydney, for UTS Tech Lab facilities and support. The authors would like to express their gratitude to Laura Jukes and the Geo-polymers and Minerals Processing Group Lab at the University of Melbourne for their assistance and provision of facilities during the course of this research.

**Conflicts of Interest:** The authors declare no conflicts of interest.

## Abbreviations

The following abbreviations are used in this manuscript:

| | |
|---|---|
| BJH | Barrett–Joyner–Halenda |
| FA | fly ash |
| FTIR | Fourier-transform infrared spectroscopy |
| GP | General Purpose |
| $LC^3$ | limestone calcined clay cement |
| OPC | ordinary Portland cement |
| PSD | particle-size distribution |
| SCM | supplementary cementitious material |
| TGA | thermogravimetric analysis |
| XRD | X-ray diffraction |

## Appendix A

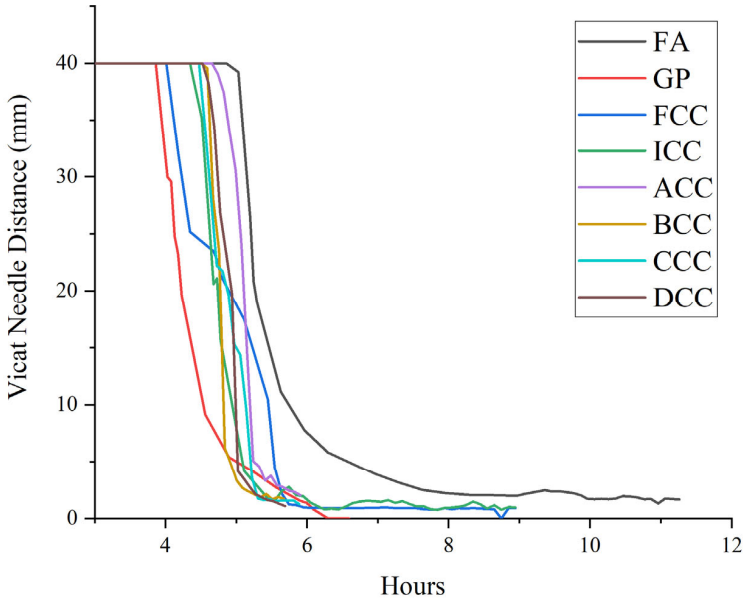


**Figure A1.** Vicat-needle setting time of each mix.

## References


1. Gagg, C.R. Cement and concrete as an engineering material: An historic appraisal and case study analysis. *Eng. Fail. Anal.* **2014**, *40*, 114–140. [CrossRef]
2. Lehne, J.; Preston, F. *Making Concrete Change: Innovation in Low-Carbon Cement and Concrete*; Chatham House: London, UK, 2018.
3. Avet, F.H. Investigation of the Grade of Calcined Clays Used as Clinker Subsitute in Limestone Calcined Clay Cement LC3.pdf. Ph.D. Thesis, École Polytechnique Fédérale de Lausanne, Lausanne, Switzerland, 2017; THÈSE NO 8143 (2017), p. 169.
4. Scrivener, K.; Martirena, F.; Bishnoi, S.; Maity, S. Calcined clay limestone cements (LC3). *Cem. Concr. Res.* **2018**, *114*, 49–56. [CrossRef]
5. Thomas, M.; Shehata, M.; Shashiprakash, S. The use of fly ash in concrete: Classification by composition. *Cem. Concr. Aggreg. (USA)* **1999**, *21*, 105–110. [CrossRef]
6. Bijen, J. Benefits of slag and fly ash. *Constr. Build. Mater.* **1996**, *10*, 309–314. [CrossRef]
7. Siddique, R.; Iqbal Khan, M. Fly Ash. In *Supplementary Cementing Materials*; Springer: Berlin/Heidelberg, Germany, 2011; pp. 1–66.
8. *Iron and Steel Technology Roadmap: Towards More Sustainable Steelmaking*; International Energy Agency: Paris, France, 2020; pp. 157–163.
9. Zunino, F.; Scrivener, K. Influence of Kaolinite Content, Limestone Particle Size and Mixture Design on Early-Age Properties of Limestone Calcined Clay Cements (LC3). In *Calcined Clays for Sustainable Concrete*; Springer: Cham, Switzerland, 2019; ICCCSC2019 Proceedings Volume 2.
10. Avet, F.; Snellings, R.; Diaz, A.A.; Ben Haha, M.; Scrivener, K. Development of a new rapid, relevant and reliable (R3) test method to evaluate the pozzolanic reactivity of calcined kaolinitic clays. *Cem. Concr. Res.* **2016**, *85*, 1–11. [CrossRef]
11. Nguyen, Q.D.; Afroz, S.; Zhang, Y.; Kim, T.; Li, W.; Castel, A. Autogenous and total shrinkage of limestone calcined clay cement (LC3) concretes. *Constr. Build. Mater.* **2022**, *314*, 125720. [CrossRef]
12. Wild, S.; Khatib, J.M.; Roose, L.J. Chemical Shrinkage and Autogenous Shrinkage of Portland Cement—Metakaolin Pastes. *Adv. Cem. Res.* **1998**, *10*, 109–119. [CrossRef]
13. Ston, J. *Basic Creep and Autogenous Shrinkage of Limestone Calcined Clay Cement ($LC^3$)*; EPFL: Lausanne, Switzerland, 2019.
14. Afroz, S.; Zhang, Y.; Nguyen, Q.D.; Kim, T.; Castel, A.; Gilbert, R.I. Shrinkage Behaviour of High Strength Slag Blended Cement-based Concrete. In Proceedings of the Concrete Institute of Australia's Biennial National Conference 2021, Perth, Australia, 5–8 September 2021; p. 4.
15. Jahren, P.; Sui, T. *History of Concrete: A Very Old and Modern Material*; World Scientific Publishing: Singapore, 2017.
16. Afroz, S.; Zhang, Y.; Nguyen, Q.D.; Kim, T.; Castel, A. Effect of limestone in General Purpose cement on autogenous shrinkage of high strength GGBFS concrete and pastes. *Constr. Build. Mater.* **2022**, *327*, 126949. [CrossRef]
17. Afroz, S.; Zhang, Y.; Nguyen, Q.D.; Kim, T.; Castel, A. Shrinkage of blended cement concrete with fly ash or limestone calcined clay. *Mater. Struct.* **2023**, *56*, 15. [CrossRef]
18. Chen, C.Y.; Lan, G.S.; Tuan, W.H. Microstructural evolution of mullite during the sintering of kaolin powder compacts. *Ceram. Int.* **2000**, *26*, 715–720. [CrossRef]
19. Kinuthia, J.M.; Wild, S.; Sabir, B.B.; Bai, J. Self-compensating autogenous shrinkage in Portland cement ± metakaolin ± fly ash pastes. *Adv. Cem. Res.* **1998**, *2000*, 35–43. [CrossRef]
20. Bouasker, M.; Khalifa, N.E.H.; Mounanga, P.; Ben Kahla, N. Early-age deformation and autogenous cracking risk of slag–limestone filler-cement blended binders. *Constr. Build. Mater.* **2014**, *55*, 158–167. [CrossRef]
21. Xu, X.; Zhao, Y.; Gu, X.; Zhu, Z.; Wang, F.; Zhang, Z. Effect of Particle Size and Morphology of Siliceous Supplementary Cementitious Material on the Hydration and Autogenous Shrinkage of Blended Cement. *Materials* **2023**, *16*, 1638. [CrossRef]
22. *AS 3972-2010*; General Purpose and Blended Cements. Standards Australia: Sydney, Australia, 2010.
23. Nguyen, Q.D.; MKhan, S.H.; Castel, A. Engineering Properties of Limestone Calcined Clay Concrete. *J. Adv. Concr. Technol.* **2018**, *16*, 343–357. [CrossRef]
24. Canda, E.; Nicolas, R.S.; Rupasinghe, M.; Rasekh, H.; Castel, A. Investigating Australian Calcined Clays as Supplementary Cementitious Materials. *Ceramics* **2025**, *8*, 9. [CrossRef]
25. *AS 3582.1*; Fly Ash. Standards Australia: Sydney, Australia, 2016.
26. *ASTM C305-20*; Standard Practice for Mechanical Mixing of Hydraulic Cement Pastes and Mortars of Plastic Consistency. ASTM: West Conshohocken, PA, USA, 2020.
27. *ASTM C-1698*; Standard Test Method for Autogenous Strain of Cement Paste and Mortar. ASTM: West Conshohocken, PA, USA, 2009.
28. Mohr, H. Influence of bleed water reabsorption on cement paste autogenous deformation. *Cem. Concr. Res.* **2010**, *40*, 220–225. [CrossRef]
29. *ASTM C191-19*; Standard Test Methods for Time of Setting of Hydraulic Cement by Vicat Needle. ASTM: West Conshohocken, PA, USA, 2019.
30. *ASTM C1608-17*; Standard Test Method for Chemical Shrinkage of Hydraulic Cement Paste. ASTM: West Conshohocken, PA, USA, 2017.

31. Zhang, T.; Gao, P.; Luo, R.; Guo, Y.; Wei, J.; Yu, Q. Measurement of chemical shrinkage of cement paste: Comparison study of ASTM C 1608 and an improved method. *Constr. Build. Mater.* **2013**, *48*, 662–669. [CrossRef]
32. Snellings, R.; Chwast, J.; Cizer, Ö.; De Belie, N.; Dhandapani, Y.; Durdzinski, P.; Elsen, J.; Haufe, J.; Hooton, D.; Patapy, C.; et al. RILEM TC-238 SCM recommendation on hydration stoppage by solvent exchange for the study of hydrate assemblages. *Mater. Struct.* **2018**, *51*, 172. [CrossRef]
33. Barrett, E.P.; Joyner, L.G.; Halenda, P.P. The Determination of Pore Volume and Area Distributions in Porous Substances. I. Computations from Nitrogen Isotherms. *J. Am. Chem. Soc.* **1951**, *73*, 373–380. [CrossRef]
34. Scrivener, K.; Snellings, R.; Lothenbach, B. *A Practical Guide to Microstructural Analysis of Cementitious Materials*; Taylor & Francis Group: Boca Raton, FL, USA, 2016.
35. Zunino, F.; Scrivener, K. The influence of the filler effect on the sulfate requirement of blended cements. *Cem. Concr. Res.* **2019**, *126*, 105918. [CrossRef]
36. Avet, F.; Scrivener, K. Investigation of the calcined kaolinite content on the hydration of Limestone Calcined Clay Cement (LC3). *Cem. Concr. Res.* **2018**, *107*, 124–135. [CrossRef]
37. Berodier, E.; Scrivener, K. Understanding the Filler Effect on the Nucleation and Growth of C-S-H. *J. Am. Ceram. Soc.* **2014**, *97*, 3764–3773. [CrossRef]
38. Dhandapani, Y.; Sakthivel, T.; Santhanam, M.; Gettu, R.; Pillai, R.G. Mechanical properties and durability performance of concretes with Limestone Calcined Clay Cement (LC3). *Cem. Concr. Res.* **2018**, *107*, 136–151. [CrossRef]
39. Bouasker, M.; Mounanga, P.; Turcry, P.; Loukili, A.; Khelidj, A. Chemical shrinkage of cement pastes and mortars at very early age: Effect of limestone filler and granular inclusions. *Cem. Concr. Compos.* **2008**, *30*, 13–22. [CrossRef]
40. Deschner, F.; Winnefeld, F.; Lothenbach, B.; Seufert, S.; Schwesig, P.; Dittrich, S.; Goetz-Neunhoeffer, F.; Neubauer, J. Hydration of Portland cement with high replacement by siliceous fly ash. *Cem. Concr. Res.* **2012**, *42*, 1389–1400. [CrossRef]
41. Afroz, S.; Kim, T.; Castel, A. Distinct Effect of Hydration of Calcined Kaolinitic Clay–Limestone Blended Cement on Microstructure and Autogenous Shrinkage. *J. Mater. Civ. Eng.* **2023**, *35*, 16184. [CrossRef]
42. Kandagaddala, R.K.; Manare, V.; Nanthagopalan, P. Limestone calcined clay as potential supplementary cementitious material—An Experimental study. In *Calcined Clays for Sustainable Concrete*; Springer: Cham, Switzerland, 2019; ICCCSC2019 Proceedings Volume 2; pp. 201–211.
43. Lothenbach, B.; Le Saout, G.; Gallucci, E.; Scrivener, K. Influence of limestone on the hydration of Portland cements. *Cem. Concr. Res.* **2008**, *38*, 848–860. [CrossRef]
44. Rossen, J.E. *Composition and Morphology of C-A-S-H in Pastes of Alite and Cement Blended with Supplementary Cementitious Materials*; EPFL: Lausanne, Switzerland, 2014.
45. Meddah, M.S.; Tagnit-Hamou, A. Pore structure of concrete with mineral admixtures and its effect on self-desiccation shrinkage. *ACI Mater. J.* **2009**, *106*, 241–250. [CrossRef]
46. Durekovic, A. Cement pastes of low water to solid ratio: An investigation of the porosity characteristics under the influence of a superplasticizer and silica fume. *Cem. Concr. Res.* **1995**, *25*, 365–375. [CrossRef]
47. Malami, C.; Kaloidas, V.; Batis, G.; Kouloumbi, N. Carbonation and porosity of mortar specimens with pozzolanic and hydraulic cement admixtures. *Cem. Concr. Res.* **1994**, *24*, 1444–1454. [CrossRef]
48. Mindess, S.; Young, J.F. *Concrete*, 1st ed.; Pearson Education: London, UK, 1981; Volume 11, pp. 639–640.
49. Hua, C.; Acker, P.; Ehrlacher, A. Analyses and models of the autogenous shrinkage of hardening cement paste: I. Modelling at macroscopic scale. *Cem. Concr. Res.* **1995**, *25*, 1457–1468. [CrossRef]
50. Song, C.; Choi, Y.C.; Choi, S. Effect of internal curing by superabsorbent polymers—Internal relative humidity and autogenous shrinkage of alkali-activated slag mortars. *Constr. Build. Mater.* **2016**, *123*, 198–206. [CrossRef]
51. Tironi, A.; Scian, A.N.; Irassar, E.F. Blended Cements with Limestone Filler and Kaolinitic Calcined Clay: Filler and Pozzolanic Effects. *J. Mater. Civ. Eng.* **2017**, *29*, 0001965. [CrossRef]
52. Barboza-Chavez, A.C.; Gomez-Zamorano, L.Y.; Acevedo-Davila, A.J.L. Synthesis and Characterization of a Hybrid Cement Based on Fly Ash, Metakaolin and Portland Cement Clinker. *Materials* **2020**, *13*, 1084. [CrossRef]
53. Yodsudjai, W.; Wang, K. Chemical shrinkage behavior of pastes made with different types of cements. *Constr. Build. Mater.* **2013**, *40*, 854–862. [CrossRef]